

Quantum-inspired interferometry with chirped laser pulses

R. Kaltenbaek,^{*} J. Lavoie, D.N. Biggerstaff, and K.J. Resch[†]
*Institute for Quantum Computing and Department of Physics & Astronomy,
 University of Waterloo, Waterloo, Canada, N2L 3G1*

We introduce and implement an interferometric technique based on chirped femtosecond laser pulses and nonlinear optics. The interference manifests as a high-visibility ($> 85\%$) phase-insensitive dip in the intensity of an optical beam when the two interferometer arms are equal to within the coherence length of the light. This signature is unique in classical interferometry, but is a direct analogue to Hong-Ou-Mandel quantum interference. Our technique exhibits all the metrological advantages of the quantum interferometer, but with signals at least 10^7 times greater. In particular we demonstrate enhanced resolution, robustness against loss, and automatic dispersion cancellation. Our interferometer offers significant advantages over previous technologies, both quantum and classical, in precision time delay measurements and biomedical imaging.

Interference is a defining feature of both quantum and classical theories of light. It also enables the most precise measurements of a wide range of physical quantities including length [1] and time [2]. Quantum metrology exploits fundamental differences between classical and quantum theories for novel measurement techniques and enhanced precision [3, 4]. Advantages stem from several phenomena associated with quantum interferometers, including nonlocal interference [5, 6], phase-insensitive interference [7], phase super-resolution and super-sensitivity [8, 9, 10], and automatic dispersion cancellation [6, 11]. Unfortunately, quantum interferometers require entangled states that are practically difficult to create, manipulate, and detect, especially compared to the ease of working with robust, intense classical states. In the present work, we show that the set of advantages previously associated with a quantum interferometer are, in fact, more easily achieved classically.

Arguably the best known example of quantum interference was demonstrated by Hong, Ou, and Mandel [7] (HOM); their interferometer is depicted in fig. 1a. HOM interference induces strong photon-photon interactions and is central to optical quantum technologies, including quantum teleportation [12] and linear-optical quantum computing [13]. Several characteristics distinguish HOM from classical interference, such as Michelsons or Youngs. The HOM signal stems from pairs of interfering photons and manifests as a dip in the rate of coincident photon detections which spans the entire coherence length of the light, as opposed to classical wavelength fringes. It is therefore inherently robust against path length fluctuations. If the photon pairs are entangled, the visibility and width of the HOM interferogram is insensitive to loss [14] and dispersion [11]. Furthermore, HOM interferometers achieve higher resolution than classical interferometers using the same bandwidth [15, 16]. These features are ideal for precision optical path measurements of dispersive and lossy materials, implemented by placing the sample in one interferometer arm and measuring the delay required to restore the dip. A quantum version of optical coherence tomography [17] (OCT) was proposed

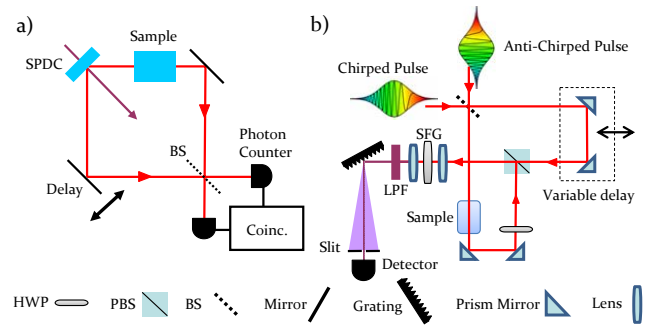


FIG. 1: Chirped-pulse interferometry. (a) The HOM interferometer. A laser of frequency $2\omega_0$ creates frequency-entangled photons through spontaneous parametric down-conversion (SPDC). The photons propagate along different paths and are recombined at a beamsplitter (BS) after one passes through a sample. The photons can arrive at different detectors when the path lengths are unbalanced; when balance is achieved, the photons always arrive at the same detector due to quantum interference. (b) The chirped-pulse interferometer. Oppositely-chirped laser pulses are combined at a beamsplitter (BS). The output beams are recombined and focused onto a nonlinear crystal after one of the beams has passed through a sample. Type-II sum frequency generation (SFG) near the frequency $2\omega_0$ as a function of delay is detected using a standard photodiode.

and demonstrated [15, 16] to harness these advantages.

Recently, two proposals [18, 19] and one experimental demonstration [20] have described classical systems exhibiting automatic dispersion cancellation. Significant drawbacks to these techniques include reliance on unavailable technology [18] or significant post-processing [19, 20]. The experimentally demonstrated technique requires wavelength path stability; the interference visibility falls precipitously with loss and is limited to 50% of that possible with the HOM effect. Alternatively, background-free autocorrelation exhibits enhanced resolution, phase insensitivity, and robustness against loss, but notably not automatic dispersion cancel-

lation; this technique has recently been used in OCT [21].

In the present work, we describe and experimentally demonstrate classical interference with *all* of the metrological advantages of the HOM interferometer. In contrast with other classical interferometers, the Feynman paths giving rise to the interference cannot be identified with the spatial paths constituting the two interferometer arms. Sum-frequency generation (SFG) acts to directly produce the interference signal from a pair of oppositely chirped optical pulses with strong classical frequency correlations; no post-processing or coincidence counting is required. The device can be understood as a time-reversed HOM interferometer using an argument [10] based on the corresponding symmetry of quantum mechanics. Remarkably, time reversal converts the quantum interferometer into a device that can use bright classical laser pulses and achieves a demonstrated ten-million-fold higher signal. Our general approach should yield similar improvements in performance when applied to many other entangled-photon based interferometers.

Hong-Ou-Mandel-based metrology can be explained using the following approach [11]. The wavevector of light in a material can be expanded about a frequency ω_0 , $k(\omega) \approx k(\omega_0) + \alpha(\omega - \omega_0) + \beta(\omega - \omega_0)^2 + \dots$, where α and β are material properties describing the group delay and quadratic group velocity dispersion (GVD), respectively. Ideal frequency-entangled photon pairs are described by the state, $|\psi\rangle = \int d\Omega f(\Omega)|\omega_0 + \Omega\rangle|\omega_0 - \Omega\rangle$, where $f(\Omega)$ is the amplitude spectrum. The coincidence rate in the HOM interferometer as a function of the relative delay time, τ , is given by [11],

$$C(\tau) = \int d\Omega |f(\Omega)|^2 \{1 - \cos[\phi_{rr}(\Omega) - \phi_{tt}(\Omega)]\}. \quad (1)$$

Here $\phi_{rr}(\Omega)$ ($\phi_{tt}(\Omega)$) are the phases associated with the amplitude where both photons are reflected (transmitted); the delay time $\tau = \frac{(L_2 - L_1 + L)}{c}$, where L_1 (L_2) is the length of the sample (delay) arm and L is the length of the sample; and $\phi_{rr}(\Omega) = L(+\alpha\Omega + \beta\Omega^2) - \Omega\tau$ and $\phi_{tt}(\Omega) = L(-\alpha\Omega + \beta\Omega^2) + \Omega\tau$, after removing an irrelevant global phase.

Since $\phi_{rr}(\Omega)$ and $\phi_{tt}(\Omega)$ have the same dependence on the GVD, β , it is automatically cancelled in the interference signal, as are all even orders of dispersion. The coincidence rate drops to zero for $\tau = \alpha L$, or when the group delay from the material is exactly compensated by unequal physical path lengths; this marks the centre of the HOM dip.

To understand our chirped-pulse interferometry (CPI) technique, consider the cross-correlator shown in fig. 1b as a time-reversed HOM interferometer (Fig. 1a). The *detection* of a pair of photons with frequencies $\omega_0 \pm \Omega$ is replaced by the *preparation* of a pair of photons with those frequencies; the *preparation* of a pump photon of frequency $2\omega_0$, which is subsequently down-converted, is replaced by the *detection* of a photon of frequency $2\omega_0$,

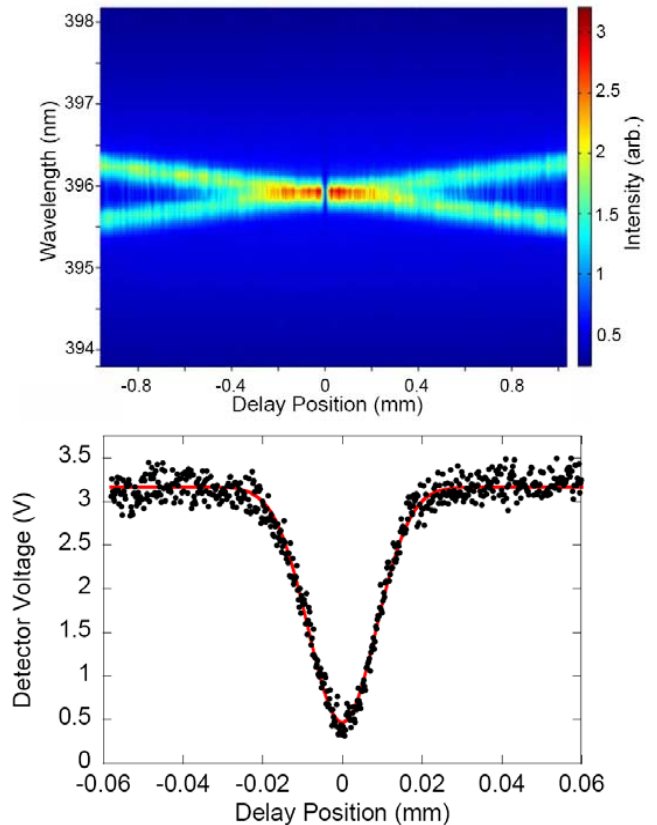


FIG. 2: Chirped-pulse interference. (a) Spectrum of the SFG versus delay position. Destructive interference removes the cross-correlation signal near zero delay; other features are discussed in the text. (b) Using a grating and a slit, we measure the optical power at 395.9nm with a bandwidth of 0.4nm, as function of delay. The signal shows a pronounced dip near zero delay; we use a Gaussian fit to measure the visibility $85.2 \pm 0.6\%$ and width $19.9 \pm 0.2\mu\text{m}$ FWHM.

which had previously been up-converted. The signal in Eq. 1 is built up by repeating the experiment with many pairs of photons with frequencies distributed according to the spectrum, $|f(\Omega)|^2$.

The power of CPI stems from the replacement of photon pairs by bright classical beams with frequencies $\omega_0 \pm \Omega$. The SFG from these beams will contain three distinct frequencies, instead of just one: the cross-correlation produces up-converted light at $2\omega_0$ at a rate proportional to $\{1 - \cos[\phi_{rr}(\Omega) - \phi_{tt}(\Omega)]\}$ (cf. Eq. 1); the autocorrelation produces two new beams at frequencies $2\omega_0 \pm 2\Omega$. A narrow bandpass filter centred at $2\omega_0$ removes the autocorrelation unless Ω is small.

The frequency difference, Ω , is swept using a pair of oppositely-chirped optical pulses with matched frequency ramps. A chirped (anti-chirped) pulse has a frequency that increases (decreases) linearly in time. We require that the chirp and anti-chirp are much greater

than any dispersion in the interferometer and stretch the pulses to many times their initial duration. Under these conditions, the input frequencies are swept in an anti-correlated manner such that at any instant only two frequencies, $\omega_0 \pm \Omega$, are input. (Oppositely-chirped pulses have previously been used to efficiently drive rotational and vibrational transitions in molecules [22, 23]). This ramp performs the integration in Eq. 1 automatically. As an added benefit, chirped pulses can have high peak intensities yielding correspondingly high frequency-conversion efficiency.

We use a modelocked ti:sapphire laser (centre wavelength 790 nm, pulse duration 110 fs, average power 2.8 W, repetition rate 80 MHz) as the light source for the experiment. The polarization of the output is rotated from vertical to horizontal using a half-wave plate to achieve maximum diffraction efficiency from our gratings. Our laser light is split using a 50/50 beamsplitter. Half of the optical power is sent through a grating-based optical compressor and the other half is sent through a grating-based optical stretcher [24, 25, 26]. The stretcher applies normal dispersion, creating a chirped pulse where the blue lags the red in time, whereas the compressor applies anomalous dispersion, creating the anti-chirped pulse where the red lags the blue. While the terms stretcher and compressor are commonly used, in our experiment both devices stretch our optical pulses. Both stretcher and compressor use 30 mm \times 30 mm, 1200 lines/mm gold-coated ruled diffraction gratings, blazed for 800nm.

In the compressor, the gratings are oriented with their faces parallel and separated by a distance of 56cm. The input beam passes over the top of a prism mirror; the retro-reflecting mirror is angled slightly downward so that the output beam is reflected by the prism mirror. The compressor produces anti-chirped output pulses 45 ± 0.1 ps long with 9nm of bandwidth and the beam has an average power of 790mW.

In the stretcher, the gratings are oriented with their faces antiparallel and separated by 145cm. A 1:1 telescope is placed between the gratings and consists of two lenses $f \approx 50$ cm separated by 98.5cm with the first lens placed 9.2cm after the first grating. The stretcher produces chirped output pulses 51.2 ± 0.2 ps long with 10nm of bandwidth and the beam has an average power of 870mW.

Initially, we balanced the stretcher and compressor by sending the output of the stretcher through the compressor and minimizing the pulse duration of the output by changing the grating separation in the compressor. We observed a minimum broadening of 10% over pulses directly from the laser. The differences between the durations of the chirped and anti-chirped pulses are due to unequal loss of bandwidth in the stretcher and compressor. They do not reflect different chirp rates.

The beams of chirped and anti-chirped pulses are injected into the cross-correlator as shown in fig. 1b. To

compensate the shorter optical path in the compressor as compared to the stretcher, the anti-chirped pulse arrives at the beamsplitter via a variable delay path (not shown). The relevant centre frequency for our experiment is not the centre frequency of the pulse, but rather is determined by the temporal overlap of the chirped and anti-chirped pulse at the 50/50 beamsplitter. If the chirped pulse lags (leads) the anti-chirped pulse, the frequency $2\omega_0$ is red-shifted (blue-shifted) from twice the centre frequency of the laser. This can be used to make measurements of group delays over a tunable range of wavelengths, which is difficult to do using HOM interference, since the entangled photons are typically produced using a fixed frequency CW laser [11, 16]. To illustrate this point, we combined our pulses such that the sum of the frequencies corresponded to a wavelength, 395.9nm, well separated from half of the centre wavelength of the laser, 395.0nm.

The two outputs from the beamsplitter travel different paths through the cross-correlator. One travels through the delay arm where a retro-reflector is placed on a motorized translation stage with 40mm travel; the other passes through the sample and an achromatic half-wave plate which rotates the polarization from horizontal to vertical. The two beams are recombined at a broadband polarizing beamsplitter cube (PBS).

The output from the PBS is focused by a 5cm achromatic lens into a 0.5mm β -barium-borate (BBO) optical crystal cut for collinear type-II degenerate sum-frequency generation. The sum-frequency beam is then collimated by means of another 5cm lens. The infrared light is filtered by means of two dichroic mirrors (not shown) designed to reflect 395nm light at 45° incidence and to transmit 790nm light, as well as a cyan coloured glass low-pass filter; this is depicted as a low-pass filter (LPF) in fig. 1b.

Fig. 2a shows the measured SFG spectrum as a function of the delay. The cross-correlation signal is clearly observed, but the autocorrelation signal comprises a broad background barely visible on this scale. For large delays, the cross-correlation signal contains two easily-discernable wavelengths spaced symmetrically about 395.9nm. These peaks arise from SFG due to the chirped component in the sample arm and the anti-chirped component in the delay arm, and vice versa. These different alternatives for producing the cross-correlation signal constitute the distributed Feynman paths which interfere. The two wavelengths approach one another as the path length difference approaches zero, where destructive interference eliminates the cross-correlation signal.

We filter a bandwidth of 0.4nm centred at 395.9nm using a 1200lines/mm aluminum-coated diffraction grating followed by a slit. The optical power is measured using an amplified silicon photodiode. The photodiode signal as a function of delay is displayed in fig. 2b and clearly

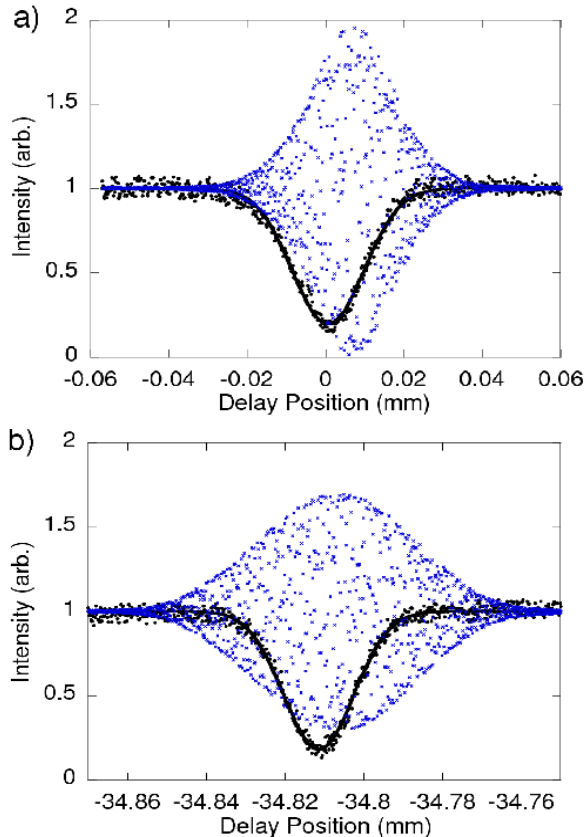


FIG. 3: Automatic dispersion cancellation in chirped-pulse interferometry. These data show a direct comparison of the chirped-pulse interference signal (black circles) and standard white-light interference using the chirped pulse (blue xs) when (a) no additional glass and (b) 80.60 ± 0.05 mm of calcite (oriented for o-polarization) and 28.93 ± 0.04 mm of BK7 glass are placed in the sample arm. Note that the small offset between the CPI and white-light interference is due to the birefringence of the up-conversion crystal.

shows the interference dip with visibility $85.2 \pm 0.6\%$ and FWHM $19.9 \pm 0.6 \mu\text{m}$ or 133 ± 1 fs.

All visibilities were calculated without background subtraction; however, our photodiode registered a bias ranging from 30 mV to 40 mV when in the dark. We measured this bias for every data set and subtracted the negative value from our measured voltage. Note that this bias correction lowers our reported visibilities.

Our measured visibility easily surpasses the 50% limit commonly attributed to any classical analogue of HOM interference. This classical limit applies only to the visibility of the coincidence rate (or correlation) between two square-law photodetector signals showing no individual interference [7, 27]. Although both SFG and coincidence detection measure correlations, the SFG signal depends on the product of the electric fields, as opposed to intensi-

ties; thus our detection scheme avoids this constraint. In practice, the background from the autocorrelation does limit the visibility, but it can be arbitrarily close to 100% with large chirp and narrow filtering. Alternatively, one could achieve 100% visibility by removing the small band of frequencies responsible for the autocorrelation background from the chirped and anti-chirped pulses; this has the drawback of distorting the interferogram.

The optical power corresponding to 1 V on our detector was measured to be $1.5 \mu\text{W}$ at 395 nm, thus our measured signal of $4.5 \mu\text{W}$ corresponds to about 10^{13} photons/s. The highest reported coincidence rate [28] from a photon pair source is 2×10^6 Hz while the rate is typically orders of magnitude lower in a HOM interferometer. Our signal is a demonstrated 7 orders of magnitude higher than what can be achieved in a HOM interferometer using state-of-the-art photon-pair sources.

To demonstrate automatic dispersion cancellation, we took two data sets: one with significant dispersive material in the sample arm, 80.60 ± 0.05 mm of calcite and 28.93 ± 0.04 mm of BK7 glass, and one without. (The dispersive properties of calcite and BK7 do not cancel, rather their effects are cumulative). In each configuration we measured chirped-pulse and white-light interferograms. To observe white-light interference, we sent the chirped pulse through the interferometer, placed a polarizer at 45° before the nonlinear crystal, and directly detected the transmitted infrared light. The resulting interferograms are shown in fig. 3a and 3b. The CPI widths and centres were obtained by a Gaussian fit whereas the white-light interference characteristics were obtained via the Hilbert transform method [29].

With no sample, fig. 3a, we observe 143 ± 2 fs FWHM for the chirped-pulse dip and 173 ± 1 fs FWHM for the white-light interference pattern. By comparing the widths we see that the chirped-pulse signal has 17% better resolution. Theory predicts an increase in resolution of 29% (assuming Gaussian bandwidths); we attribute the difference to the acceptance bandwidth of our SFG crystal, the offset of our chirped-pulse average wavelength from our pulse centre wavelength, and the slightly unequal bandwidths of our chirped and anti-chirped pulses. With the dispersive elements, fig. 3b, we observed 140 ± 2 fs FWHM for chirped-pulse interference and 303 ± 2 fs FWHM for white-light interference. Dispersion clearly increased the width of the white-light interference pattern by 75%; the width of the chirped-pulse interference pattern remained essentially unchanged due to dispersion cancellation.

To show that CPI accurately determines group delays, we measured shifts in the centre of the interference of $34811.9 \pm 0.3 \mu\text{m}$ and $34813.80 \pm 0.3 \mu\text{m}$ for the chirped-pulse dip and white-light fringes respectively. These agree well with theoretical shifts of $34816 \pm 20 \mu\text{m}$ and $34822 \pm 20 \mu\text{m}$, calculated from the group delays at 791.8 nm and 790 nm, respectively. Uncertainties in the

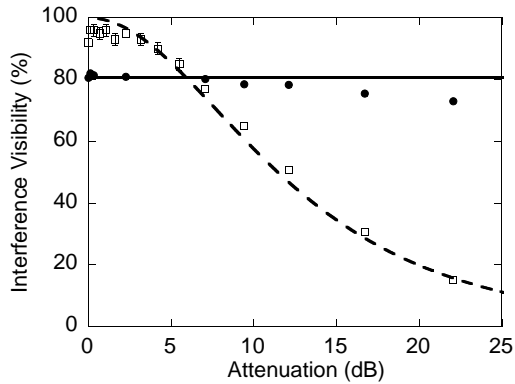


FIG. 4: Visibility versus unbalanced loss. These data show the visibility of the chirped-pulse interference dip (closed circles, solid line theory) and white-light interference (open squares, dashed line theory) as a function of loss in the sample arm introduced by rotating the half-wave plate (Fig. 1b). The chirped-pulse interference visibility shows far more resilience to loss. Error bars indicate statistical errors of 1 s.d.

theory result from errors in the measurement of sample thickness.

A further advantage of CPI as compared to white-light interferometry is the insensitivity of the visibility to unbalanced loss in the interferometer arms; loss will, however, reduce the overall output intensity, and thus the signal, in both cases. We measured both visibilities as a function of attenuation in the sample path. Rotating a half-wave plate in the sample path enables continuous adjustment of the loss at the polarizing beam splitter. The results of these measurements are shown in fig. 4. The visibility in the chirped-pulse interference is far more robust than the white-light interference, dropping only slightly at high attenuation due solely to background. This insensitivity can be explained by noting that in CPI the loss is common to both interfering Feynman paths even though it is localized in one physical path.

Chirped-pulse interferometry features all of the metrological advantages of Hong-Ou-Mandel interference with vastly higher signal levels. CPI achieves this without the inherent disadvantages of entangled photon sources and single-photon detection. Increasing the laser bandwidth and the spectral acceptance of sum-frequency generation [30] will make CPI resolution competitive with that in optical coherence tomography [17, 31]. Automatic dispersion cancellation, enhanced resolution, and insensitivity to loss and path length fluctuations promise to make CPI a superior imaging technology, especially for dispersive and lossy media, e.g. biological specimens and photonic devices. More generally, our work emphasizes the importance of delineating truly quantum effects from those with classical analogue [11, 32, 33], and shows how quantum insights can inspire novel classical technologies. Our approach provides an avenue into previ-

ously untapped potential of classical interferometry.

We thank D. Strickland for sharing invaluable expertise on pulse compression techniques and K. Bizheva and G. Weihs for important discussions and loaning equipment. We thank J. Sanderson, J. Lundeen, M. Mitchell, J. Gambetta, A. White, and A. Steinberg for helpful comments. This work was supported by NSERC, and CFI. D.B. and R.K. acknowledge financial support from the Mike and Ophelia Lazaridis Fellowship and IQC, respectively.

* Electronic address: rkaltenb@iqc.ca

† Electronic address: kresch@iqc.ca

- [1] B. Abbott, R. Abbott, R. Adhikari, J. Agresti, P. Ajith, B. Allen, J. Allen, R. Amin, S. B. Anderson, W. G. Anderson, et al., *Phys. Rev. Lett.* **95**, 221101 (2005).
- [2] T. Udem, J. Reichert, R. Holzwarth, and T. W. Hänsch, *Phys. Rev. Lett.* **82**, 3568 (1999).
- [3] H. Lee, P. Kok, and J. P. Dowling, *J. Mod. Opt.* **49**, 2325 (2002).
- [4] V. Giovannetti, S. Lloyd, and L. Maccone, *Science* **306**, 1330 (2004).
- [5] J. D. Franson, *Phys. Rev. Lett.* **62**, 2205 (1989).
- [6] J. D. Franson, *Phys. Rev. A* **45**, 3126 (1992).
- [7] C. K. Hong, Z. Y. Ou, and L. Mandel, *Phys. Rev. Lett.* **59**, 2044 (1987).
- [8] P. Walther, J.-W. Pan, M. Aspelmeyer, R. Ursin, S. Gasparoni, and A. Zeilinger, *Nature* **429**, 158 (2004).
- [9] M. W. Mitchell, J. S. Lundeen, and A. M. Steinberg, *Nature* **429**, 161 (2004).
- [10] K. J. Resch, K. L. Pregnell, R. Prevedel, A. Gilchrist, G. J. Pryde, J. L. O'Brien, and A. G. White, *Phys. Rev. Lett.* **98**, 223601 (2007).
- [11] A. M. Steinberg, P. G. Kwiat, and R. Y. Chiao, *Phys. Rev. Lett.* **68**, 2421 (1992).
- [12] D. Bouwmeester, J.-W. Pan, K. Mattle, M. Eibl, H. Weinfurter, and A. Zeilinger, *Nature* **390**, 575 (1997).
- [13] E. Knill, R. Laflamme, and G. J. Milburn, *Nature* **409**, 46 (2001).
- [14] A. M. Steinberg, P. G. Kwiat, and R. Y. Chiao, *Phys. Rev. Lett.* **71**, 708 (1993).
- [15] A. F. Abouraddy, M. B. Nasr, A. V. S. B. E. A. Saleh, and M. C. Teich, *Phys. Rev. A* **65**, 053817 (2002).
- [16] M. B. Nasr, B. E. A. Saleh, A. V. Sergienko, and M. C. Teich, *Phys. Rev. Lett.* **91**, 083601 (2003).
- [17] J. G. Fujimoto, M. E. Brezinski, G. J. Tearney, S. A. Boppart, and B. Bouma, *Nat. Med.* **1**, 970 (1995).
- [18] B. I. Erkmen and J. H. Shapiro, *Phys. Rev. A* **74**, 041601 (2006).
- [19] K. Banaszek, A. S. Radunsky, and I. A. Walmsley, *Opt. Comm.* **269**, 152 (2007).
- [20] K. J. Resch, P. Puvanathan, J. S. Lundeen, M. W. Mitchell, and K. Bizheva, *Opt. Express* **15**, 8797 (2007).
- [21] A. Pe'er, Y. Bromberg, B. Dayan, Y. Silberberg, and A. A. Friesem, *Opt. Express* **15**, 8760 (2007).
- [22] J. Karczmarek, J. Wright, P. Corkum, and M. Ivanov, *Phys. Rev. Lett.* **82**, 3420 (1999).
- [23] J. F. Xia, J. H. Sanderson, W.-K. Liu, and D. Strickland, *J. Phys. B: AMO Phys.* **36**, L409 (2003).

- [24] E. B. Treacy, *Quantum Electron.* **QE-5**, 454 (1969).
- [25] O. E. Martínez, *IEEE J. Quantum Electron.* **24**, 2530 (1988).
- [26] M. Pessot, P. Maine, and G. Mourou, *Opt. Comm.* **62**, 419 (1987).
- [27] H. Paul, *Rev. Mod. Phys.* **58**, 209 (1986).
- [28] J. Altepeter, E. Jeffrey, and P. Kwiat, *Opt. Express* **13**, 8951 (2005).
- [29] A. F. Fercher, W. Drexler, C. K. Hitzenberger, and T. Lasser, *Rep. Prog. Phys.* **66**, 239 (2003).
- [30] S. Carrasco, M. B. Nasr, A. V. Sergienko, B. E. Saleh, M. C. Teich, J. P. Torres, and L. Torner, *Opt. Lett.* **31**, 253 (2006).
- [31] W. Drexler, *J. Biomed. Opt.* **9**, 47 (2004).
- [32] R. S. Bennink, S. J. Bentley, and R. W. Boyd, *Phys. Rev. Lett.* **89**, 113601 (2002).
- [33] F. Ferri, D. Magatti, A. Gatti, M. Bache, E. Brambilla, and L. A. Lugiato, *Phys. Rev. Lett.* **94**, 183602 (2005).